PHYSICAL REVIEW D **72,** 084022 (2005)

Numerical integration of the Teukolsky equation in the time domain

Enrique Pazos-Ávalos* and Carlos O. Lousto

Department of Physics and Astronomy, and Center for Gravitational Wave Astronomy, The University of Texas at Brownsville, Brownsville, Texas 78520, USA

(Received 16 September 2004; revised manuscript received 22 September 2005; published 24 October 2005)

We present a fourth-order convergent, (2 + 1)-dimensional, numerical formalism to solve the Teukolsky equation in the time domain. Our approach is first to rewrite the Teukolsky equation as a system of first-order differential equations. In this way we get a system that has the form of an advection equation. This is then used in combination with a series expansion of the solution in powers of time. To obtain a fourth-order scheme we kept terms up to fourth derivative in time and use the advectionlike system of differential equations to substitute the temporal derivatives by spatial derivatives. This scheme is applied to evolve gravitational perturbations in the Schwarzschild and Kerr backgrounds. Our numerical method proved to be stable and fourth-order convergent in r^* and θ directions. The correct power-law tail, $\sim 1/t^{2\ell+3}$, for general initial data, and $\sim 1/t^{2\ell+4}$, for time-symmetric data, was found in our runs. We noted that it is crucial to resolve accurately the angular dependence of the mode at late times in order to obtain these values of the exponents in the power-law decay. In other cases, when the decay was too fast and round-off error was reached before a tail was developed, then the quasinormal modes frequencies provided a test to determine the validity of our code.

DOI: 10.1103/PhysRevD.72.084022 PACS numbers: 04.25.Dm, 04.25.Nx, 04.30.Db, 04.70.Bw

I. INTRODUCTION

In recent years, there has been an increasing interest in numerically solving general relativity's (GR) field equations to provide an accurate description of the gravitational radiation generated in different astrophysical scenarios. This is due mainly to fact that direct measure of gravitational waves will soon be possible with large interferometers such as LIGO and LISA. The astrophysical events that produce gravitational waves are among the most energetic phenomena ever seen. The best candidate for such observations are the collision of binary black hole systems. In order to detect this gravitational radiation, accurate templates are needed, and this implies to solve the nonlinear GR equations. This proved to be a very challenging task. Although in the last orbital stages (merger) of a binary black hole collision it is necessary to solve GR's field equations (full numerical approach), in the very last part of the coalescence (close limit) the system can be considered as a single distorted black hole and can be treated with perturbation theory. Comparisons between full numerical simulations and perturbative methods show a surprisingly good agreement. This has encouraged researchers to go beyond and implement a matching of the close limit and full numerical simulations in tandem to produce simulations that neither of each technique alone was able to do. The general method of coupling full numerical and approximate techniques is one of the main development of the "Lazarus project" [1–5].

There are physical scenarios in which the metric departure from the known static black hole solutions is always small outside the event horizon. Some examples are a particle (compact object) orbiting a black hole, and the propagation of gravitational waves and accretion disks around black holes. The equations evolved in the perturbative method are linear which is an advantage over the nonlinear set of ten coupled general relativistic equations.

One application of perturbation theory is the propagation of waves in a curved spacetime. In this work, we will focus our study in the late time behavior of a gravitational wave in such curved space-times. Although the problem is not new, according to Andersson [6] there are still some aspects for which there is no definite answer or no answers at all; like the role played by highly damped modes and the intermediate behavior of the power-law tails. Power-law tails is the name given to the last phase in the propagation of a wave in a curved background, as we will see below. The general features of the evolution of such a test field in the proximity of a black hole, as seen by a distant observer, can be divided into three stages: (i) Radiation emitted directly by the perturbation source. It depends on the form of the initial field (initial data). (ii) Quasinormal ringing. It depends on the parameters of the black hole. They are exponentially damped oscillations and carry part of the gravitational radiated energy in astrophysical processes like gravitational collapse. Quasinormal modes are characterized by complex frequencies σ. Such modes can be represented as $e^{i\sigma t}$, the real part of σ is the oscillation frequency and the imaginary part is the exponential damping. (iii) Power-law tail. The field decays with time according to a power-law at very late times.

Most of the work on the late time radiative falloff has been done in spherically symmetric space-times. In this case the solution admits a decomposition in spherical harmonics. The field equations are reduced to a wave equation with an effective potential. For the

---

*On leave from the Universidad de San Carlos de Guatemala.

1550-7998/2005/72(8)/084022(18)$23.00

Schwarzschild case this wave equation is

$$\left[-\frac{\partial^2}{\partial t^2}+\frac{\partial^2}{\partial r^{*2}}-V_\ell^{\pm}(r)\right]\Psi^{\pm}_{\ell m}(t,r)=0, \tag{1.1}$$

where r^* is the tortoise coordinate

$$r^* = r + 2M\ln(r/2M-1), \tag{1.2}$$

M the mass of the black hole, and

$$V_\ell^+ = 2\left(1-\frac{2M}{r}\right) \times \frac{[\lambda^2(\lambda+1)r^3+3\lambda^2Mr^2+9\lambda M^2r+9M^3]}{r^3(\lambda r+3M)^2}, \tag{1.3}$$

$$V_\ell^- = 2\left(1-\frac{2M}{r}\right)\left(\frac{\lambda+1}{r^2}-3\frac{M}{r^3}\right), \tag{1.4}$$

are the Zerilli's and Regge-Wheeler potentials, respectively, and where $\lambda = (\ell-1)(\ell+2)/2$. ℓ being the multipole index.

In 1972, Price [7] treated Eq. (1.1) as a perturbative expansion in powers of M. He showed that the perturbation decays in time according to $t^{-(2\ell+3)}$ for $t \gg r \gg M$. This situation occurs at a finite value of r while $t \longrightarrow \infty$.

Quasinormal modes and power-law tails have been studied by Leaver [8], who analyzed the problem in the frequency domain. He found the correct late time behavior with a low-frequency approximation. Quasinormal modes can be considered as the ''pure tones'' of the black hole. Once excited, their damping and oscillation frequency depend only on the parameters of the black hole. Ching *et al.* [9] argue that the late time decay of the field can be seen as a scattering due to the spacetime curvature. This implies that the power-law behavior depends only on the asymptotic conditions of the metric. In a recent work, Poisson [10] found that in a weakly curved spacetime the late time dynamics is insensitive to the nonspherical aspects of the metric, being entirely determined by the spacetime total mass.

In Ref. [11] it is found that the power-law tails are not an universal phenomenon as originally thought, but the falloff power depends on the initial profile of the fields. While for the generic data with $\Phi_\ell|^{t=0} \neq 0$ and $\partial_t\Phi_\ell|^{t=0} \neq 0$ the predicted [7] decay goes like $1/t^{2\ell+3}$, when one starts with an initially static scalar field, i.e. $\Phi_\ell|^{t=0} \neq 0$ and $\partial_t\Phi_\ell|^{t=0} = 0$ the predicted decay goes like $1/t^{2\ell+4}$.

Most of the work with the Teukolsky equation has been performed in the frequency domain (quasinormal modes, wave scattering, motion of test particles). Perturbation on the frequency domain can be reduced analytically to solve ordinary differential equations and can lead to a better understanding of the physics involved in the phenomena. Such information is much more difficult to obtain from purely numerical computations. However, in general, the number of frequencies that one needs to consider for nonquasicircular orbits is large, being very difficult to reach high accuracy. Furthermore, the study of quasinormal modes would require higher resolution near $\omega = 0$ to resolve the tails. The resolution of the quasinormal modes is also sensitive to the spacing in frequencies. These are the argument presented by Krivan *et al.* [12] in favor of a numerical treatment of perturbations using the Teukolsky equation in the time domain. Another motivation to work in the time domain is that when one tries to find a solution of the radial Teukolsky equation in the frequency domain with a source term that extends to infinity, the result is divergent. This means that the Teukolsky equation needs to be regularized when sources are present [13,14].

The difficulty with numerical integrations of the Teukolsky equation is the linear term in s on the first time derivative (See Eq. (1.6) below). Depending on the relative sign between this term and the second time derivative, it can act as a damping or antidamping term. As described in [12], stable time evolutions are achieved by writing the Teukolsky equation as a set of first-order differential equations. This and other issues concerning the implementation of a fourth-order algorithm are discussed in the next section. Our motivations for developing a fourth-order convergent algorithm are mainly that it can reproduce the same accurate results of a second-order convergent code with less resolution. This makes the former to run faster than the later. Although in a fourth-order scheme, more intense computation is needed, there is some gain in speed when equivalent effective resolutions, i.e. resolutions that produce the same error in the solution, are used. On the other hand, if equal resolutions are used, a fourth-order method will yield more accurate solutions. The price one has to pay in this case is that the fourth-order method will take longer to finish the run. This issues enter into consideration in gravitational wave detection, because of the large number of templates needed for data analysis. The gain in accuracy can also be used in second-order perturbation theory, since higher order derivatives of the field are needed to build up the effective source term [15]. This may also have important applications in the ''Lazarus approach'' [1] and the radiation reaction problem of a particle orbiting a black hole [16,17] . Fourth-order full numerical relativity has recently been implemented [18] bearing in mind these motivations, and a fourth-order numerical algorithm has recently been developed to deal with nonvacuum (particle like) perturbations of Schwarzschild black holes [19].

Using the Kinnersley null tetrad

$$\begin{aligned} \boldsymbol{l} &= [(r^2+a^2)/\Delta, 1, 0, a/\Delta], \\ \mathbf{n}^\mu &= [r^2+a^2, -\Delta, 0, a]/(2\Sigma), \\ \mathbf{m}^\mu &= [ia\sin\theta, 0, 1, i\sin\theta]/[\sqrt{2}(r+ia\cos\theta)], \mu \end{aligned} \tag{1.5}$$

where $\Sigma = r^2 + a^2\cos^2\theta$ and $\Delta = r^2 - 2Mr + a^2$, the

Newman-Penrose equations written in Boyer-Lindquist coordinates lead to the Teukolsky equation [20]

$$\begin{aligned}&\left[\frac{(r^2+a^2)^2}{\Delta}-a^2\sin^2\theta\right]\partial_{tt}\Psi+\frac{4Mar}{\Delta}\partial_{t\phi}\Psi\\&+2s\left[r-\frac{M(r^2-a^2)}{\Delta}+ia\cos\theta\right]\partial_t\Psi-\Delta^{-s}\partial_r(\Delta^{s+1}\partial_r\Psi)\\&-\frac{1}{\sin\theta}\partial_\theta(\sin\theta\partial_\theta\Psi)-\left[\frac{1}{\sin^2\theta}-\frac{a^2}{\Delta}\right]\partial_{\phi\phi}\Psi\\&-2s\left[\frac{a(r-M)}{\Delta}+\frac{i\cos\theta}{\sin^2\theta}\right]\partial_\phi\Psi+(s^2\cot^2\theta-s)\Psi=4\pi\Sigma T.\end{aligned} \tag{1.6}$$

The gravitational perturbations are recovered setting $s = \pm 2$, s is a parameter called *spin weight*. Here the quantities of interest are related to the Weyl scalars $\Psi = \rho^{-4}\psi_4$ with $\rho = -1/(r - ia\cos\theta)$ for $s = -2$, and $\Psi = \psi_0$ for $s = +2$.

It is well known that (1.6) can be separated in the frequency domain by taking $\Psi = e^{-i\omega t}e^{im\phi}S(\theta; a\omega)R(r)$. When $s = 0$, the functions $S(\theta)$ are the spheroidal functions. When $a\omega = 0$ these eigenfunctions are the spin weighted spherical harmonics ${}_sS_\ell^m(\theta, 0)e^{im\phi} = {}_sY_\ell^m(\theta, \phi)$. The general solution can then be represented as

$$\Psi = \int d\omega \sum_{\ell,m} R(r)_m^\ell \ {}_sS_\ell^m(\theta; a\omega)e^{im\phi}e^{i\omega t}. \tag{1.7}$$

In most astrophysical applications, we are interested in computing solutions that represent gravitational radiation at infinity. This information is carried out by ψ_4. This, together with the good asymptotic behavior of the solutions, are the motivations of choosing the value $s = -2$ to perform the time evolutions. Knowing the value of ψ_4 allows us to calculate the outgoing energy flux per unit time as [15]

$$\frac{dE}{du} = \lim_{r\to\infty}\left[\frac{r^2}{4\pi}\int_\Omega d\Omega \left|\int_{-\infty}^{u} d\tilde{u}\psi_4(\tilde{u}, r, \theta, \phi)\right|^2\right], \tag{1.8}$$

where $d\Omega = \sin\theta d\theta d\phi$ and $u = t - r$.

In the next section we explicitly give the numerical techniques used to solve the Teukolsky equation starting from a review of the second-order convergent formalism developed in Ref. [12]. We then derive the fourth-order accurate in time and space algorithm, as a natural generalization of the Lax-Wendroff method. We finish Sec. II with a description of the radiative boundary conditions imposed to the field in the two radial boundaries and the angular boundary conditions imposed by the symmetry of the solution (along the z axis). Section III deals with the applications of the fourth-order code. As initial data we consider an outgoing Gaussian pulse located in the far region. The fourth-order convergence in both spatial variables is verified in Sec. III B. We then compute the quasinormal modes and power-law tails as an ultimate test of the code. Finally we discuss some of the consequences of the computed decay powers on the light of ongoing discussion in the literature.

II. NUMERICAL TECHNIQUES

A. Review

In this work we will follow the approach used by Krivan *et al.* [12]. They integrate the Teukolsky equation in the time domain by rewriting it as a set a first-order partial differential equations. The aim of their work is the evolution of gravitational perturbations of Kerr's spacetime. This is explicitly done for the case $s = -2$. This choice is due to the fact that we are interested in radiation reaching $r^* \to \infty$. The asymptotic behavior of the solutions of (1.6), for a given spin weight s, representing ingoing and outgoing waves is [12,20]

$$\lim_{r^*\to+\infty}|\Psi_s| \sim \begin{cases} 1/r^{2s+1} & \text{for outgoing,} \\ 1/r & \text{for ingoing,} \end{cases} \tag{2.1}$$

$$\lim_{r^*\to-\infty}|\Psi_s| \sim \begin{cases} 1 & \text{for outgoing,} \\ \Delta^{-s} & \text{for ingoing.} \end{cases} \tag{2.2}$$

The procedure of solving the Teukolsky equation for $s = -2$ is initiated by introducing the ansatz

$$\Psi(t, r^*, \theta, \tilde{\phi}) = \sum_m r^3 e^{im\tilde{\phi}}\Phi(t, r^*, \theta; m), \tag{2.3}$$

where r^* is the Kerr tortoise coordinate, defined as

$$dr^* = \frac{r^2 + a^2}{\Delta}dr. \tag{2.4}$$

So[1],

$$\begin{aligned} r^* &= r + \frac{r_+^2 + a^2}{r_+ - r_-}\ln\left|\frac{r - r_+}{2M}\right| - \frac{r_-^2 + a^2}{r_+ - r_-}\ln\left|\frac{r - r_-}{2M}\right|, \\ r_\pm &= M \pm \sqrt{M^2 - a^2}, \end{aligned} \tag{2.5}$$

and $\tilde{\phi}$ is the Kerr azimuthal coordinate, defined as

$$d\tilde{\phi} = d\phi + \frac{a}{\Delta}dr. \tag{2.6}$$

So,

$$\tilde{\phi} = \phi + \frac{a}{r_+ - r_-}\ln\left|\frac{r - r_+}{r - r_-}\right|. \tag{2.7}$$

Next it is introduced an auxiliary field Π defined as

$$\Pi \equiv \partial_t\Phi + b\partial_{r^*}\Phi, \tag{2.8}$$

where

---

[1] Note that in the literature it is also used a different normalization for the two logarithmic terms instead of $2M = r_+ + r_-$ it appears r_+ and r_- respectively.

$$b \equiv \frac{r^2 + a^2}{\Sigma}, \tag{2.9}$$

and

$$\Sigma^2 \equiv (r^2 + a^2)^2 - a^2 \Delta \sin^2\theta. \tag{2.10}$$

This decomposes the second-order differential Teukolsky Eq. (1.6) into a system of first-order differential equations. The resulting equation can be expressed in matrix form

$$\partial_t \mathbf{u} + \mathbf{M}\partial_{r^*}\mathbf{u} + \mathbf{L}\mathbf{u} + \mathbf{A}\mathbf{u} = 0, \tag{2.11}$$

where $\mathbf{u} \equiv (\Phi_R, \Phi_I, \Pi_R, \Pi_I)^T$ is a column vector whose components are the real and imaginary (R, I) parts of the fields Φ and Π. The coefficients involving derivatives in (1.6) are rearranged as the elements of matrices $\mathbf{M}$ and $\mathbf{A}$, given by

$$\mathbf{M} \equiv \begin{bmatrix} b & 0 & 0 & 0 \\ 0 & b & 0 & 0 \\ m_{31} & m_{32} & -b & 0 \\ -m_{32} & m_{31} & 0 & -b \end{bmatrix}, \tag{2.12}$$

and

$$\mathbf{A} \equiv \begin{bmatrix} 0 & 0 & -1 & 0 \\ 0 & 0 & 0 & -1 \\ a_{31} & a_{32} & a_{33} & a_{34} \\ -a_{32} & a_{31} & -a_{34} & a_{33} \end{bmatrix}. \tag{2.13}$$

The remaining matrix $\mathbf{L}$ contains the derivatives of the fields with respect to the polar coordinate θ, whose components are

$$\mathbf{L} \equiv \begin{bmatrix} 0 & 0 & 0 & 0 \\ 0 & 0 & 0 & 0 \\ l_{31} & 0 & 0 & 0 \\ 0 & l_{31} & 0 & 0 \end{bmatrix}. \tag{2.14}$$

The values of each element of the above matrices are given in the Appendix of Ref. [12] and are corrected here in Eqs. (2.35), (2.44), (2.45), (2.46), (2.47), (2.48), and (2.49) below.

We next proceed to solve the first-order system (2.11) using the Lax-Wendroff method [21]. For this, (2.11) is rewritten as

$$\partial_t \mathbf{u} + \mathbf{D}\partial_{r^*}\mathbf{u} = \mathbf{S}, \tag{2.15}$$

where $\mathbf{D} = \mathrm{diag}(b, b, -b, -b)$ and $\mathbf{S} = -(\mathbf{M} - \mathbf{D})\partial_{r^*}\mathbf{u} - \mathbf{L}\mathbf{u} - \mathbf{A}\mathbf{u}$.

To solve the above equation in Ref. [12] it was used a grid with 8000 points for r^* and 32 points for θ. The computational domain was $-100M \leq r_i^* \leq 500M$ and $0 \leq \theta_j \leq \pi$, with a Courant condition of $\delta t \leq \min(\delta r^*, 5\delta\theta)$.

Boundary conditions have been imposed as follows: $\Phi = \Pi = 0$ at the horizon and outer boundary. Along the axis, $\Phi = 0$ or $\partial_\theta \Phi = 0$ for m, (the azimuthal number) odd or even, respectively.

With these settings Ref. [12] code showed stability for the order of $1000M$ of evolution time. It was reported second-order convergent for times $<50M$, and with a convergence rate higher than 1.3 for later times.

In the following sections we will focus on generalizing the numerical algorithm to accomplish a fourth-order convergent numerical evolution, using the first-order formulation of the Teukolsky equation (2.11) as the starting point.

B. Rewriting Teukolsky equation

1. Separating ϕ dependence

The Teukolsky equation is separable in the azimuthal variable for the general case of $s \neq 0$ and $a \neq 0$. Furthermore, we will change the normal Boyer-Lindquist coordinates r and ϕ into r^* and $\tilde{\phi}$, respectively. This has the advantage that as r approaches asymptotically to r_+ the coordinate r^* goes to minus infinity, so the inner boundary of the computational domain is approximated very close to the horizon, but still outside the black hole.

The variable $\tilde{\phi}$ is used to improve the behavior of the coordinates near the horizon. This is a manifestation of the frame dragging effect of a rotating black hole [22].

Now we make use of the ansatz (2.3) used by Krivan *et al.*, where they also include a factor r^3. This is done to eliminate the increasing behavior of the solutions at infinity, according to (2.1). So we substitute (2.3) into (1.6), setting the source term $T = 0$ to get vacuum space solutions. After dropping a global $r^3 e^{im\tilde{\phi}}$ factor we get

$$\begin{aligned} &-\left[\frac{(r^2 + a^2)^2}{\Delta} - a^2 \sin^2\theta\right]\partial_{tt}\Phi + \frac{2}{\Delta}[Ms(r^2 - a^2) - rs\Delta - ia(s\Delta\cos\theta + 2Mmr)]\partial_t\Phi + \frac{(r^2 + a^2)^2}{\Delta}\partial_{r^*r^*}\Phi \\ &\quad + \frac{1}{r\Delta}[(8r^2 + 6a^2)\Delta - 2rs(r^2 + a^2)(M - r) + 2iamr(r^2 + a^2)]\partial_{r^*}\Phi + \partial_{\theta\theta}\Phi + \cot\theta\partial_\theta\Phi \\ &\quad + \frac{1}{r^2\Delta}\{6\Delta^2 - r\Delta[6M(s + 1) - r(7s + 6) + r(s\cot\theta + m\csc\theta)^2] - 2iamr[2rs(M - r) - 3\Delta]\} = 0. \end{aligned} \tag{2.16}$$

We can bring this equation into the form

$$\begin{aligned} \partial_{tt}\Phi + C_t\partial_t\Phi + C_{r^*r^*}\partial_{r^*r^*}\Phi + C_{r^*}\partial_{r^*}\Phi + C_{\theta\theta}\partial_{\theta\theta}\Phi \\ + C_\theta\partial_\theta\Phi + C_{\mathrm{so}}\Phi = 0, \end{aligned} \tag{2.17}$$

where the C's are (We simply multiply by $-\Delta/\Sigma^2$.)

$$C_t = 2s\frac{M(a^2 - r^2) + r\Delta}{\Sigma^2} + 2ia\frac{2mMr + s\Delta\cos\theta}{\Sigma^2} \tag{2.18}$$

$$C_{r^*r^*} = -\frac{(r^2+a^2)^2}{\Sigma^2}, \tag{2.19}$$

$$C_{r^*} = 2\frac{rs(M-r)(r^2+a^2)-(3a^2+4r^2)\Delta}{r\Sigma^2} - 2iam\frac{r^2+a^2}{\Sigma^2}, \tag{2.20}$$

$$C_{\theta\theta} = -\frac{\Delta}{\Sigma^2}, \tag{2.21}$$

$$C_{\theta} = -\frac{\Delta}{\Sigma^2}\cot\theta, \tag{2.22}$$

$$C_{\mathrm{so}} = 2iam\frac{2rs(M-r)-3\Delta}{r\Sigma^2} + \Delta\frac{6Mr(s+1)-r^2(7s+6)-6\Delta+r^2(s\cot\theta+m\csc\theta)^2}{r^2\Sigma^2}. \tag{2.23}$$

2. From second to first-order differential equations

A common technique to numerically solve a second-order differential equation is to rewrite it as a set of first-order differential equations and then apply the appropriate methods. We hence want to write (2.17) as an advection equation with a source term

$$\begin{bmatrix}\Phi\\ \Pi\end{bmatrix}_{,t} + \begin{bmatrix}\beta_{11} & \beta_{12}\\ \beta_{21} & \beta_{22}\end{bmatrix}\begin{bmatrix}\Phi\\ \Pi\end{bmatrix}_{,r^*} + \begin{bmatrix}\gamma_{11} & \gamma_{12}\\ \gamma_{21} & \gamma_{22}\end{bmatrix}\begin{bmatrix}\Phi\\ \Pi\end{bmatrix} = \mathbf{0}, \tag{2.24}$$

where none of the β's and γ's depend on t. Expanding the matrix products we get two (complex) equations

$$\partial_t\Phi + \beta_{11}\partial_{r^*}\Phi + \beta_{12}\partial_{r^*}\Pi + \gamma_{11}\Phi + \gamma_{12}\Pi = 0, \tag{2.25}$$

$$\partial_t\Pi + \beta_{21}\partial_{r^*}\Phi + \beta_{22}\partial_{r^*}\Pi + \gamma_{21}\Phi + \gamma_{22}\Pi = 0. \tag{2.26}$$

Now let $\beta_{12} = \gamma_{11} = 0$ and $\gamma_{12} = -1$. By doing this we obtain an expression for Π that depends only on the derivatives of Φ with respect to t and r^* (and some function β_{11})

$$\Pi = \partial_t\Phi + \beta_{11}\partial_{r^*}\Phi, \tag{2.27}$$

which is similar to (2.8), but β_{11} has not yet been specified. We will see that with this definition, Π can be easily substituted and eliminated in the second equation (2.26). The derivatives of Π are

$$\partial_t\Pi = \partial_{tt}\Phi + \beta_{11}\partial_{tr^*}\Phi \tag{2.28}$$

$$\partial_{r^*}\Pi = \partial_{r^*t}\Phi + (\partial_{r^*}\beta_{11})(\partial_{r^*}\Phi) + \beta_{11}\partial_{r^*r^*}\Phi. \tag{2.29}$$

Substituting (2.27), (2.28), and (2.29), into (2.26) and rearranging terms we find

$$\partial_{tt}\Phi - \gamma_{22}\partial_t\Phi - (\beta_{11}+\beta_{22})\partial_{r^*t}\Phi + \beta_{22}\beta_{11}\partial_{r^*r^*}\Phi - (\beta_{21} - \beta_{22}\partial_{r^*}\beta_{11} - \gamma_{22}\beta_{11})\partial_{r^*}\Phi - \gamma_{21}\Phi = 0. \tag{2.30}$$

To find the value of the β's and γ's we equate the coefficients of the derivatives of Φ in (2.30) with those in (2.17). From the coefficient of $\partial_{r^*t}\Phi$ we find that $\beta_{22} = -\beta_{11}$. Combining this with the coefficient of $\partial_{r^*r^*}\Phi$ we see that $\beta_{11} = \sqrt{-C_{r^*r^*}}$

$$-\beta_{22} = \beta_{11} = \frac{r^2+a^2}{\Sigma} = b. \tag{2.31}$$

This is exactly the definition of b in (2.9). It is easy to show that the remaining equations yield the following results

$$\gamma_{22} = C_t, \tag{2.32}$$

$$\gamma_{21} = C_{\mathrm{so}} + l_{31}, \tag{2.33}$$

$$\beta_{21} = C_{r^*} + b\partial_{r^*}b - C_t b. \tag{2.34}$$

Here l_{31} is defined according to (2.14) as the θ-derivative operator

$$l_{31} = C_{\theta\theta}\partial_{\theta\theta} + C_\theta\partial_\theta, \tag{2.35}$$

in the sense that it can be "factored" as $l_{31}\Phi$ and added to $C_{\mathrm{so}}\Phi$. Of course, an expression as (2.33) is not mathematically rigorous. It is rather a way to express that the equation's angular dependence is going to be added to the source term. Furthermore, in a numerical implementation we do not compute the value of γ_{21}, but the value of $\gamma_{21}\Phi$.

3. Splitting real and imaginary parts

Because the Teukolsky equation involves complex coefficients it is necessary to treat the real and imaginary parts of the solution. Let us define four functions Φ_R, Φ_I, Π_R and Π_I, such that

$$\Phi = \Phi_R + i\Phi_I, \tag{2.36}$$

$$\Pi = \Pi_R + i\Pi_I, \tag{2.37}$$

and substitute them into (2.25) and (2.26). After collecting real and imaginary parts and equating both to zero, we obtain a set of four equations. As a shorthand to denote derivatives, we use a dot for ∂_t and a prime for ∂_{r^*}

$$\dot\Phi_R + b\Phi'_R - \Pi_R = 0, \tag{2.38}$$

$$\dot\Phi_I + b\Phi'_I - \Pi_I = 0, \tag{2.39}$$

$$\dot\Pi_R + \beta^R_{21}\Phi'_R - \beta^I_{21}\Phi'_I - b\Pi'_R + \gamma^R_{21}\Phi_R - \gamma^I_{21}\Phi_I + C^R_t\Pi_R - C^I_t\Pi_I = 0, \tag{2.40}$$

$$\dot{\Pi}_I + \beta^I_{21}\Phi'_R + \beta^R_{21}\Phi'_I - b\Pi'_I + \gamma^I_{21}\Phi_R + \gamma^R_{21}\Phi_I + C^I_t\Pi_R + C^R_t\Pi_I = 0. \quad (2.41)$$

We can finally arrange these equations in matrix form as follows

$$\begin{bmatrix}\Phi_R\\ \Phi_I\\ \Pi_R\\ \Pi_I\end{bmatrix}_t + \begin{bmatrix} b & 0 & 0 & 0\\ 0 & b & 0 & 0\\ \beta^R_{21} & -\beta^I_{21} & -b & 0\\ \beta^I_{21} & \beta^R_{21} & 0 & -b\end{bmatrix}\begin{bmatrix}\Phi_R\\ \Phi_I\\ \Pi_R\\ \Pi_I\end{bmatrix}_{r^*} + \begin{bmatrix} 0 & 0 & -1 & 0\\ 0 & 0 & 0 & -1\\ \gamma^R_{21} & -\gamma^I_{21} & C^R_t & -C^I_t\\ \gamma^I_{21} & \gamma^R_{21} & C^I_t & C^R_t\end{bmatrix}\begin{bmatrix}\Phi_R\\ \Phi_I\\ \Pi_R\\ \Pi_I\end{bmatrix} = \mathbf{0}. \quad (2.42)$$

Comparing this last equation with (2.11) and making use of our definitions of β_{21} and γ_{21}, Eqs. (2.33) and (2.34), respectively; we see that this derivation yields the same structure for the Teukolsky equation as that derived by Krivan *et al.* [12]. Although the structure of the equation is the same, the coefficients shown above do not completely agree with those of Ref. [12]. The coefficients that do not agree are $C_{\rm so}$ and the real part of C_{r^*}, which correspond to what Ref. [12] calls c_2, c_5 and c_6. The coefficients reported in [12] correspond to the case in which the ansatz for the solution is

$$\Psi(t, r^*, \theta, \tilde{\phi}) = \sum_m e^{im\tilde{\phi}}\Phi(t, r^*, \theta; m). \quad (2.43)$$

Note that this equation does not contain the function r^3 used in (2.3). Another correction that needs to be done in order to recover the Teukolsky equation is to set $a_{31} = -c_5$ and $a_{34} = -c_3$, in the definitions presented in Ref. [12], Eqs. (A8).

Summarizing, the coefficients used in this paper, using the ansatz (2.3) are

$$\beta^R_{21} = m_{31} = 2\frac{rs(M-r)(r^2+a^2) - (3a^2+4r^2)\Delta}{r\Sigma^2} - 2bs\frac{M(a^2-r^2)+r\Delta}{\Sigma^2} + b\partial_{r^*}b, \quad (2.44)$$

$$\beta^I_{21} = -m_{32} = -2am\frac{r^2+a^2}{\Sigma^2} - 2ba\frac{2mMr + s\Delta\cos\theta}{\Sigma^2}, \quad (2.45)$$

$$\gamma^R_{21} = a_{31} + l_{31} = \frac{\Delta}{r^2\Sigma^2}(6Mr(s+1) - r^2(7s+6) - 6\Delta + r^2(s\cot\theta + m\csc\theta)^2) - \frac{\Delta}{\Sigma^2}\partial_{\theta\theta} - \frac{\Delta}{\Sigma^2}\cot\theta\partial_\theta, \quad (2.46)$$

$$\gamma^I_{21} = -a_{32} = 2am\frac{2rs(M-r) - 3\Delta}{r\Sigma^2}, \quad (2.47)$$

$$C^R_t = a_{33} = 2s\frac{M(a^2-r^2)+r\Delta}{\Sigma^2}, \quad (2.48)$$

$$C^I_t = -a_{34} = 2a\frac{2mMr + s\Delta\cos\theta}{\Sigma^2}. \quad (2.49)$$

Direct comparison with the coefficients (A1)–(A8) published in Ref. [12] shows the differences above mentioned.

C. Derivation of the 4th order algorithm

Let us assume that the function $u(t, x)$ has continuous derivatives in both t and x up to order four in some given interval and that this function satisfies a differential equation of the form

$$u_t = vu_x, \quad (2.50)$$

where v is a constant and the subscripts represent first derivatives with respect to t and x respectively. The Taylor expansion in t for $u(t, x)$ is

$$u(t+\delta t, x) = u + u_t\delta t + u_{tt}\frac{\delta t^2}{2!} + u_{ttt}\frac{\delta t^3}{3!} + u_{tttt}\frac{\delta t^4}{4!} + \cdots. \quad (2.51)$$

Here u and its derivatives are evaluated at some given slice (t_0, x). Now we can use Eq. (2.50) to replace the time derivatives by spatial derivatives, using the fact that $u_{tt} = v^2u_{xx}$, $u_{ttt} = v^3u_{xxx}$ and so on. Thus we have

$$u(t+\delta t, x) = u + vu_x\delta t + v^2u_{xx}\frac{\delta t^2}{2!} + v^3u_{xxx}\frac{\delta t^3}{3!} + v^4u_{xxxx}\frac{\delta t^4}{4!} + \cdots. \quad (2.52)$$

If we truncate this series, taking terms up to δt^2 we will obtain the Lax-Wendroff scheme, which is second-order accurate in space and time. Introducing the usual discrete notation U^n_j for $u(t_n, x_j)$ and using a second-order accurate approximation for x derivatives we have [23]

$$U^{n+1}_j = U^n_j - \alpha(U^n_{j+1} - U^n_{j-1}) + \frac{1}{2}\alpha^2(U^n_{j+1} - 2U^n_j + U^n_{j-1}), \quad (2.53)$$

where $\alpha = v\delta t/\delta x$.

In order to have a fourth-order accurate scheme, we truncate the Taylor expansion of $u(t, x)$ including terms up to δt^4 and using the differential equation (2.50) to replace time derivatives by space derivatives. Furthermore, we use a fourth-order finite difference scheme (see Appendix B) to approximate spatial derivatives. Proceeding in this way we have

$$\begin{aligned} U_j^{n+1} = {} & U_j^n + \frac{\alpha}{12}(U_{j-2}^n - 8U_{j-1}^n + 8U_{j+1}^n - U_{j+2}^n) - \frac{\alpha^2}{24}(U_{j-2}^n - 16U_{j-1}^n + 30U_j^n - 16U_{j+1}^n + U_{j+2}^n) \\ & + \frac{\alpha^3}{48}(U_{j-3}^n - 8U_{j-2}^n + 13U_{j-1}^n - 13U_{j+1}^n + 8U_{j+2}^n - U_{j+3}^n) - \frac{\alpha^4}{144}(U_{j-3}^n - 12U_{j-2}^n + 39U_{j-1}^n - 56U_j^n \\ & + 39U_{j+1}^n - 12U_{j+2}^n + U_{j+3}^n). \end{aligned} \tag{2.54}$$

Note that the dependence on the discretization parameters δt and δx appears as powers of α.

D. Boundary conditions

1. Radial boundary conditions

We use Sommerfeld boundary conditions at radial infinity and at the event horizon. When one uses the tortoise coordinate r^* the event horizon is reached when $r^* \longrightarrow -\infty$. In practice, it turns that setting $r^* = -50M$ is a good approximation. For this value we have $|r - r_H| \approx 10^{-12}$. At the inner boundary, the condition is that of an ingoing wave

$$\frac{\partial}{\partial t}\Phi(t, r^*, \theta) = \frac{\partial}{\partial r^*}\Phi(t, r^*, \theta). \tag{2.55}$$

At the outer boundary, the appropriate condition is that of an outgoing wave

$$\frac{\partial}{\partial t}\Phi(t, r^*, \theta) = -\frac{\partial}{\partial r^*}\Phi(t, r^*, \theta). \tag{2.56}$$

In order to make this conditions compatible with our fourth-order integration scheme, we take higher derivatives of (2.55) and (2.56). The idea is again, to substitute the time derivatives of the Taylor expansion (2.51) by means of the boundary conditions above. The results are summarized in Table I.

The implementation of boundary conditions is straightforward when a second-order scheme is employed. This is due to the fact that we only need up to second-order spatial derivatives and its stencil demands only 3 points.[2] On the other hand, the case of a fourth-order accurate expression for spatial derivatives needs two more points for the first derivative and seven points for the fourth derivative, see Appendix B. So, in this case, the way we implemented the radial boundary conditions is to use off-centered expressions to compute the spatial derivatives, when needed. Assuming a computational grid of $N_r + 1$ points in the r^* direction, labeling the points from 0 to N_r, Table II shows the points for which off-centered spatial derivatives are used.

As to the auxiliary field Π, defined in (2.8), its boundary condition follows directly from its definition and from (2.55) and (2.56). Once we know the boundary values for Φ, the value for Π at the inner boundary is

$$\Pi = \partial_t\Phi + b\partial_{r^*}\Phi = (b + 1)\partial_{r^*}\Phi \tag{2.57}$$

where we have used (2.55) and b is given by (2.9). In a similar way, the outer boundary condition is

$$\Pi = (b - 1)\partial_{r^*}\Phi. \tag{2.58}$$

2. Angular boundary conditions

These are imposed along the rotation axis, i.e. at $\theta = 0$ and $\theta = \pi$. The boundary condition depends on the particular azimuthal mode m (see Eq. (2.3)) chosen for the evolution, it can be stated as

$$\Phi = 0 \quad \text{for} \quad m = \pm 1, \pm 3, \pm 5... \tag{2.59}$$

$$\partial_\theta\Phi = 0 \quad \text{for} \quad m = 0, \pm 2, \pm 4... \tag{2.60}$$

These conditions come directly from the dependence of the spheroidal harmonics on θ. At the same time it is precisely this behavior that we use in order to implement the appropriate boundary conditions. The solutions for which m is even, have even parity about both, $\theta = 0$ and $\theta = \pi$. On the other hand, the solutions with odd m, have odd parity about $\theta = 0$ and $\theta = \pi$, i.e.

$$\left.\begin{array}{rcl} \Phi(t, r^*, \theta) & = & \Phi(t, r^*, -\theta) \\ \Phi(t, r^*, \pi + \theta) & = & \Phi(t, r^*, \pi - \theta) \end{array}\right\} \text{for} \;\; m = 0, \pm 2, ... \tag{2.61}$$

$$\left.\begin{array}{rcl} \Phi(t, r^*, \theta) & = & -\Phi(t, r^*, -\theta) \\ \Phi(t, r^*, \pi + \theta) & = & -\Phi(t, r^*, \pi - \theta) \end{array}\right\} \text{for} \;\; m = \pm 1, \pm 3, ... \tag{2.62}$$

TABLE I. Boundary conditions for the radial direction.

Inner boundary $r^* = r^*_{\min}$	Outer boundary $r^* = r^*_{\max}$
$\partial_t\Phi = \partial_{r^*}\Phi$	$\partial_t\Phi = -\partial_{r^*}\Phi$
$\partial_t^2\Phi = \partial_{r^*}^2\Phi$	$\partial_t^2\Phi = \partial_{r^*}^2\Phi$
$\partial_t^3\Phi = \partial_{r^*}^3\Phi$	$\partial_t^3\Phi = -\partial_{r^*}^3\Phi$
$\partial_t^4\Phi = \partial_{r^*}^4\Phi$	$\partial_t^4\Phi = \partial_{r^*}^4\Phi$

---

[2] For centered finite differences, a second-order accurate formula needs two points to compute first derivatives and three points for second derivatives.

TABLE II. Points for which off-centered derivatives in the r^* direction are used (point labeling: $N_r + 1$ points from 0 to N_r).

Off-centered derivatives	used at points
∂_{r^*}, $\partial^2_{r^*}$	1, $N_r - 1$
$\partial^3_{r^*}$, $\partial^4_{r^*}$	1, 2, $N_r - 1$, $N_r - 2$

To take advantage of this property we need to use a staggered grid in the θ direction. By doing this we also avoid the inherent difficulties of evaluating expressions in which $\cot\theta$ is present, (like the last term of Teukolsky Eq. (1.6)) since this function is not finite neither at $\theta = 0$ nor $\theta = \pi$. In a staggered grid, the values for $\theta = 0$ and $\theta = \pi$ are always located exactly between two grid points. The points to the left (right) of $\theta = 0$ ($\theta = \pi$) are considered as "ghost zones", because are used just to implement the boundary conditions. In our fourth-order method, we need four ghost points. Two before the first point $\theta = 0$ and two more after the point $\theta = \pi$, as shown in Fig. 1. Our grid has $N_\theta + 3$ points in the θ direction, the first two and last two points are ghost points. In this way we can always use a centered formula to compute the derivatives in the θ direction. Notice that if we are using a second-order accurate approximation, we only need one ghost point at each end of the grid. The values in the ghost zones are updated according to (2.61) and (2.62).

E. Notes on implementation

We mention here some implementation details of Eq. (2.11), which for convenience will be written as[3]

$$\partial_t \mathbf{u} = -\mathbf{M}\partial_{r^*}\mathbf{u} - (\mathbf{L} + \mathbf{A})\mathbf{u}. \tag{2.63}$$

As stated above, the main idea has been always to substitute the time derivatives in the Taylor expansion (2.51) by spatial derivatives using our differential Eq. (2.63). Calling $\mathbf{G} = -(\mathbf{L} + \mathbf{A})$, all time derivatives needed are

$$\partial_t \mathbf{u} = -\mathbf{M}\partial_{r^*}\mathbf{u} + \mathbf{G}\mathbf{u}, \tag{2.64}$$

$$\partial_t^2 \mathbf{u} = -\mathbf{M}\partial_{r^*}(\partial_t \mathbf{u}) + \mathbf{G}(\partial_t \mathbf{u}), \tag{2.65}$$

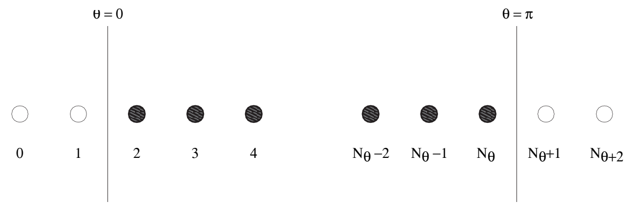

FIG. 1. White circles: ghost zones, black circles: normal grid points

$$\partial_t^3 \mathbf{u} = -\mathbf{M}\partial_{r^*}(\partial_t^2 \mathbf{u}) + \mathbf{G}(\partial_t^2 \mathbf{u}), \tag{2.66}$$

$$\partial_t^4 \mathbf{u} = -\mathbf{M}\partial_{r^*}(\partial_t^3 \mathbf{u}) + \mathbf{G}(\partial_t^3 \mathbf{u}). \tag{2.67}$$

Here we have used the fact that none of the coefficients of the Teukolsky equation are time dependent and that partial derivatives commute.

The four time derivatives above could be computed using just the finite differences formula for the first derivative in r^*. Once we know $\partial_t \mathbf{u}$ we can *numerically* substitute this result to get the second time derivative $\partial_t^2 \mathbf{u}$ and so on. The problem with this procedure is that because of the exclusive use of the first r^* derivative formula; at the end, we will not have a fourth r^* derivative with the accuracy shown in Appendix B. It still will be fourth-order accurate but using the first derivative formula 4 times will propagate more error than that of the fourth-order accurate finite differences formula. The same holds for the other derivatives. The approach we took was to compute all time derivatives directly from the coefficients of the evolution equation, and the value of the fields at every time step. Of course, this implies much more larger expressions to compute time derivatives, because now we have to *algebraically* substitute one time derivative into the other. Carrying out such a substitutions we find

$$\partial_t \mathbf{u} = -\mathbf{M}\mathbf{u}' + \mathbf{G}\mathbf{u}, \tag{2.68}$$

$$\partial_t^2 \mathbf{u} = \mathbf{M}[\mathbf{M}'\mathbf{u}' - (\mathbf{G}\mathbf{u})' + \mathbf{M}\mathbf{u}''] + \mathbf{G}\partial_t \mathbf{u}, \tag{2.69}$$

$$\begin{aligned}\partial_t^3 \mathbf{u} &= -\mathbf{M}\{(\mathbf{G}\partial_\mathbf{t}\mathbf{u})' + \mathbf{M}'^2\mathbf{u}' - \mathbf{M}'[(\mathbf{G}\mathbf{u})' + \mathbf{3} - \mathbf{M}\mathbf{u}''] - \mathbf{M}[\mathbf{u}' - \mathbf{M}'' + (\mathbf{G}\mathbf{u})'' - \mathbf{M}\mathbf{u}^{(3)}]\} + \mathbf{G}\partial_\mathbf{t}^2\mathbf{u},\ \partial_\mathbf{t}^4\mathbf{u}\\ &= -\mathbf{M}\{(\mathbf{G}\partial_\mathbf{t}^2\mathbf{u})' - \mathbf{M}'^3\mathbf{u}' + \mathbf{M}'^2((\mathbf{G}\mathbf{u})' + \mathbf{7} - \mathbf{M}\mathbf{u}'') - \mathbf{M}'[(\mathbf{G}\partial_\mathbf{t}\mathbf{u})' - \mathbf{M}(\mathbf{4}\mathbf{u}' - \mathbf{M}'' + \mathbf{3}(\mathbf{G}\mathbf{u})'' + \mathbf{6} - \mathbf{M}\mathbf{u}^{(3)})]\\ &\quad - \mathbf{M}[(\mathbf{G}\mathbf{u})' - \mathbf{M}'' + (\mathbf{G}\partial_\mathbf{t}\mathbf{u})'' - \mathbf{M}(\mathbf{4} - \mathbf{M}''\mathbf{u}'' + \mathbf{u}' - \mathbf{M}^{(3)} + (\mathbf{G}\mathbf{u})^{(3)} - \mathbf{M}\mathbf{u}^{(4)})]\} + \mathbf{G}\partial_\mathbf{t}^3\mathbf{u}.\end{aligned}$$

To simplify the equations, we have used "primes" to denote differentiation with respect to r^*.

There is one final point, worthwhile mentioning here. Notice that there are still some products in which the time derivatives of $\mathbf{u}$ and $\mathbf{u}$ itself appear explicitly. All of these products involve products with $\mathbf{G}$. Neither the time derivatives nor $\mathbf{u}$ are algebraically substituted in these products because $\mathbf{G} = -(\mathbf{L} + \mathbf{A})$ and $\mathbf{L}$ contains the θ derivatives operator. Instead of expanding further derivatives, we chose to numerically substitute the time derivatives of $\mathbf{u}$ and $\mathbf{u}$ itself into these products. We use the term "numerically substitute" in the sense that each time derivative is calculated and stored in the memory of the computer,

---

[3] We use lower case bold face to denote vectors and upper case bold face to denote matrices.

further computation makes use of the stored values. Such a procedure gives good results as shown in the next section.

III. RESULTS

A. Initial data

In all runs (unless otherwise specified), initial data with compact support was used. The function used was a Gaussian bell centered at $r^* = 75M$, in the asymptotic r^* direction and some (ℓ, m) mode dependence in the θ direction. Thus, for $t = 0$ we have

$$\Phi(0, r^*, \theta) = e^{-(r^*-75)^2/100}\Theta_{\ell m}(\theta) \tag{3.1}$$

where $\Theta_{\ell m}(\theta)$ represents the θ dependence as spherical harmonics $Y_\ell^m(\theta, \phi)$ or the spin weighted spherical harmonics $sY_\ell^m(\theta, \phi)$; for $s = 0$ and $s = -2$, respectively. Table III shows the θ dependence of the spherical harmonics and spin weighted spherical harmonics for $m = 0$ up to a value of $\ell = 4$. We also need to specify the initial value of $\partial_t\Phi$ to evaluate the auxiliary function Π defined in (2.27). Asymptotically an outgoing pulse satisfies the condition $\partial_t\Phi = -\partial_{r^*}\Phi$. Thus, using this relation in (2.27), the initial value of the time derivative is implemented as the initial value of Π

$$\Pi(0, r^*, \theta) = (b - 1)\partial_{r^*}\Phi(0, r^*, \theta). \tag{3.2}$$

B. Fourth-order convergence

Convergence was tested in both r^* and θ directions simultaneously. The method to assess convergence was to compare four runs for the same initial data but with different resolutions. The way of varying resolutions was such that they kept the same ratio. If we identify successive resolutions for both, r^* and θ as δ_1, δ_2, $\delta_3 \ldots \delta_n$ in ascending order; they satisfy

$$\frac{\delta_i}{\delta_{i+1}} = \rho, \tag{3.3}$$

where $\rho > 1$. In practice, this ratio was taken to be 1.5 or 2. Each time the resolution is increased, the numerical solution must converge to the true solution. In absence of an analytical solution we took the one obtained with the finer resolution and compute the differences between this and the other three, in which lower resolution was used. The relation between the true and numerical solution, (for a given resolution up to the leading order) is

$$\Psi_{\text{num}} = \Psi_{\text{true}} + k\delta_i^4 + \cdots \tag{3.4}$$

where in general $k = k(r, \theta)$. From this it is easy to show that the differences between the numerical solutions are scaled by the fourth power of the resolution (see the figures for the actual value of the scale factor).

Figures. 2–4 show fourth-order convergence in the r^* direction. The simulation parameters are (in all runs the black hole mass was taken as $M = 1$ and the Courant factor was 0.5)

The radial and angular resolutions are increased by a factor of 3/2. Using this factor creates a minor problem that needs to be solved before computing the differences of the four numerical solutions. The problem is that the discrete set of values of the variables are completely different when resolution is changed. This fact is illustrated in Fig. 5 for the case of the θ variable (where there is also the effect of the staggered grid). Therefore, in order to assess convergence, we used a sixth order Lagrange polynomial to interpolate the solution obtained with the finer resolutions at the values r_j^* and θ_k of the coarse one. Figure 2 shows the differences, in absolute value, of the higher resolution run and the three other. It corresponds to the instant $t = 200M$. The initial pulse is approximately outgoing, so during the evolution there is a small perturbation that travels towards the black hole, originated by the initial pulse. By this time, this perturbation has bounced off the potential barrier and has reached a maximum amplitude of $\sim 6 \times 10^4$. A rough estimation indicates an error of 0.08% at the highest amplitude. Figure 3 shows the same phase than the previous one but at $t = 900M$. The error has increased now to $\sim$0.6%. A careful examination of Fig. 3 shows that the difference between the three lines is more notorious than in Fig. 2. That means that the convergence rate is less than 4, but it is still consistent with a rate of 3.95. Figure 4 shows

TABLE III. θ dependence of Y_ℓ^0 and ${}_{-2}Y_\ell^0$ without the normalization constant.

ℓ-mode	${}_0Y_\ell^0$	${}_{-2}Y_\ell^0$
$\ell = 0$	1	–
$\ell = 1$	$\cos\theta$	–
$\ell = 2$	$3\cos^2\theta - 1$	$\sin^2\theta$
$\ell = 3$	$5\cos^3\theta - 3\cos\theta$	$\cos\theta\sin^2\theta$
$\ell = 4$	$35\cos^4\theta - 30\cos^2\theta + 3$	$(5 + 7\cos 2\theta)\sin^2\theta$

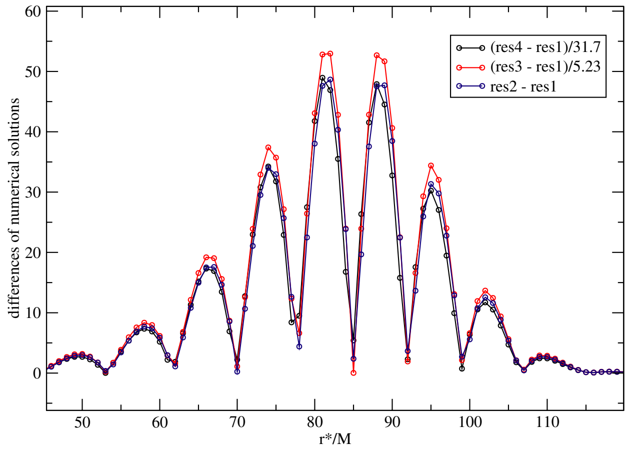

FIG. 2 (color online). Convergence test in r^* at $\theta = \pi/2$ and $t = 200M$.

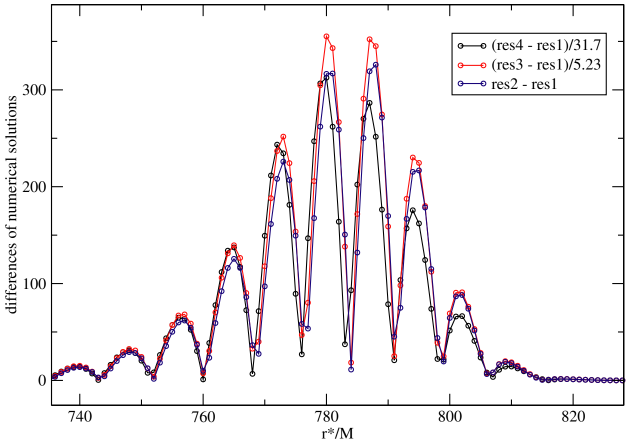

FIG. 3 (color online). Convergence test in r^* at $\theta = \pi/2$ and $t = 900M$.

the same phase of the previous two graphs at different time steps. It is clear that the relative error increases linearly with time.

As to the convergence in the θ direction, Fig. 6 shows fourth-order convergence for a fixed value of $r^* = 20M$. The simulation parameters are being the same as those for the r^* analysis. The amplitude decreases as the wave passes by. The graph shows different snapshots at intervals of $200M$. Convergence is lost when round-off error is reached.

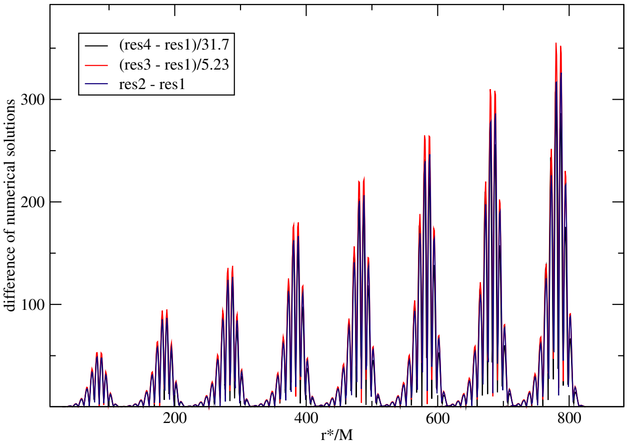

FIG. 4 (color online). Convergence test in r^* at $\theta = \pi/2$ at time intervals of $100M$.

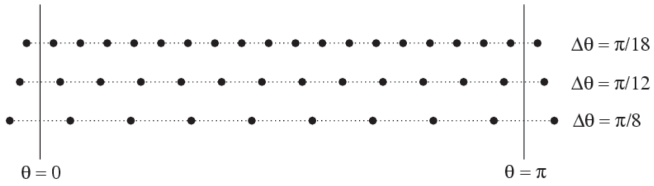

FIG. 5. Distribution of the grid points θ_k for different resolutions (Only one ghost point shown here.)

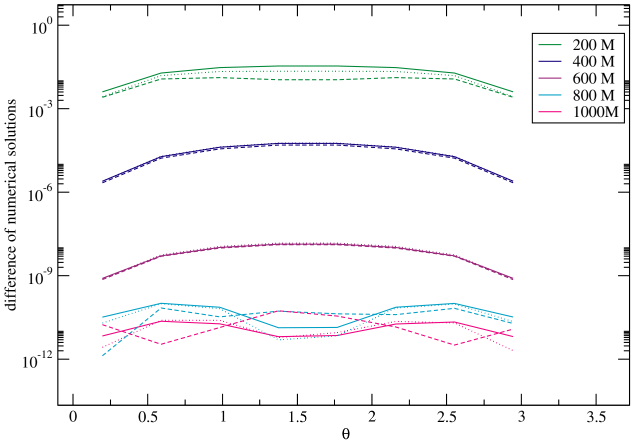

FIG. 6 (color online). Convergence test in θ at $r^* = 20M$ at time intervals of $200M$. The continuous lines represents the difference (res2-res1), the dashed one represents (res3 - res1)/5.23 and the dotted is (res4-res1)/31.7. The resolutions res1, res2, res3 and res4 are $\pi/27$, $\pi/18$, $\pi/12$, $\pi/8$; respectively

Other test performed to check the validity of the numerical solutions was evolving the initial data of a known analytic function. This function does not need to be a solution of the Teukolsky equation, it could be any smooth function in r^* and θ, provided that the corresponding source term is added to the evolution equations. The idea is the following: Let us call $\mathcal{T}$ the "Teukolsky operator" so that $\mathcal{T}[\Phi(t, r^*, \theta)] = 0$ is the Teukolsky equation (2.16). If we choose an arbitrary smooth function $\tilde{\Phi}(t, r^*, \theta)$, the result of applying the operator $\mathcal{T}$ will be

$$\mathcal{T}(\tilde{\Phi}(t, r^*, \theta)) = f(t, r^*, \theta). \qquad (3.5)$$

If we add the source term $f(t, r^*, \theta)$ to the evolution equations and give the initial data as $\tilde{\Phi}(0, r^*, \theta)$ and $\partial_t\tilde{\Phi}(0, r^*, \theta)$ our code should reproduce the function $\tilde{\Phi}$. In Fig. 7 we show the result of such a test. We set the function $\tilde{\Phi}$ as a Gaussian pulse (in r^* and θ), traveling in the increasing direction of r^*. Our code reproduce the analytic function with high accuracy. Note that there is some damping in the amplitude of the pulse due to numerical dispersion though.

C. Power-law tails

One of the main applications of this work is to accurately compute the power-law falloff in the evolution of the gravitational perturbations. In the following results the observation point is located at $r^* = 20M$ and $\theta = \pi/2$. The highest resolution used was $\delta r^* = 0.125M$, $\delta\theta = \pi/48$ and the lowest one was $\delta r^* = 1M$, $\delta\theta = \pi/8$. Variation of the resolution in those intervals was done in

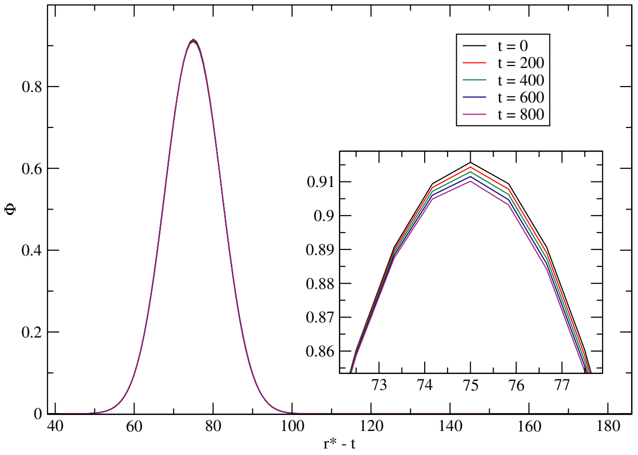

FIG. 7 (color online). Snapshots of an outgoing Gaussian pulse. Numerical dispersion effects appear at late times (space and time are in units of M).

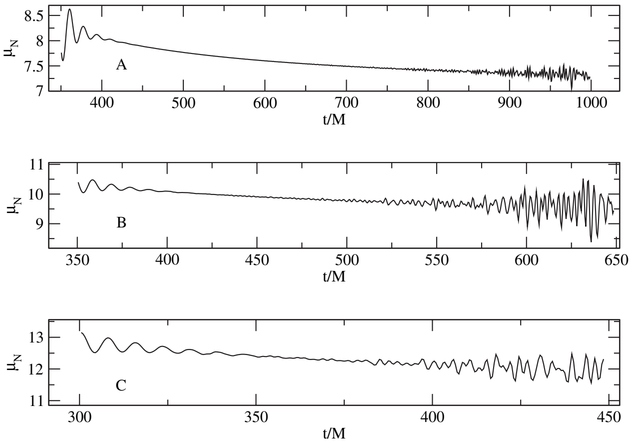

FIG. 8. Local power index μ_N for $m = 0$, $a = 0$. Part A, B and C correspond to ℓ values of 2, 3 and 4;, respectively, with their corresponding power-law tails of 7, 9 and 11.

order to verify convergence, although the lowest resolution was not good enough in cases where the θ profile presents several oscillations. Computationally, the determination of power-law tails is a challenging problem, because the amplitude of the wave decays exponentially during quasinormal ringing and as an inverse power of time during the tail phase. This means that we are working with very small numbers that eventually reach round-off error, due to the finite precision of the computer processor. This posses some difficulties when we try to determine the exponent of the power-law. Recall that at very late times, for a finite value of r^*, the amplitude of the field goes as

$$\Phi \propto t^{-(2\ell+3)}. \tag{3.6}$$

In principle, finding this exponent should not be a problem since a simple power fitting of the form $\Phi = At^{-\mu}$ (where A and μ are constants) would be just fine. The problem with this procedure is that (3.6) behavior is at the very last stage in the evolution of the perturbation. In practice, we are not able to evolve the perturbations for such a long time, due to the finiteness of computational resources[4]. So we analyze the field Φ just from the moment the tail phase begins until the moment the solution reaches round-off error. During this period, the field falloff is governed also by powers of time smaller than $-(2\ell + 3)$ [24]

$$\Phi \propto t^{-\mu} + O(t^{-(\mu+n)}), \tag{3.7}$$

which means that the exponent of t reaches $-(2\ell + 3)$ in an asymptotic way. The "local power index" [25] defined as $\mu_N = -t\partial_t\Phi/\Phi$ is a good method to see that the tails approach asymptotically to the theoretical value. This is shown in Fig. 8. We notice that the larger the value of ℓ the shorter the interval of validity for μ_N. This is due to the fact that for larger values of ℓ, the power-law exponent is bigger (in absolute value), making the field to decay very fast reaching round-off error earlier. Figure 9 shows this behavior for $m = 0$, $a = 0$ and different values of ℓ. A closer examination to Figs. 8 and 9 reveals that the oscillations in μ_N start some time before round-off error appears. The origin of such behavior is attributed to the accumulated numerical error that increases as the evolution progresses. This oscillations are magnified in Fig. 8 due to the numerical time derivatives of the field Φ.

Based on this behavior we are interested in computing the exponent of the next term in the right hand side of (3.7). For this, we did a series of nonlinear fits to a model of the form

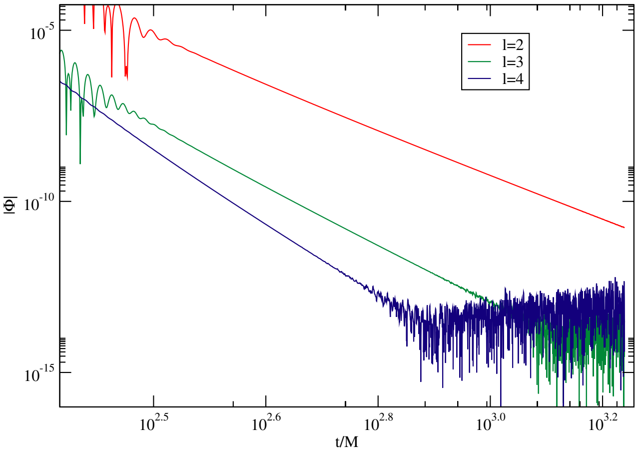

FIG. 9 (color online). Power-law tails for $m = 0$, $a = 0$ and different values of ℓ. The evolution time is $1600M$ with a resolution $\delta r^* = 0.25M$ and $\delta\theta = 0.098$.

---

[4] In our case this finiteness is precisely RAM memory. This is because the outer boundary condition is not perfect and after some finite time, part of the initial pulse is reflected back. To delay the arrival of this reflection the outer boundary must be far away from the observation point, which means a large computational domain; in other words: more RAM memory.

$$\Phi = A/t^{\mu} + B/t^{\mu+n}, \tag{3.8}$$

where the adjustable parameters are A, B and μ. The parameter n is a positive integer (the cases considered are for $s = -2$ and $a = 0$). The results are shown in Table IV. We see immediately that the best fitted value of the power-law tail μ is obtained when $n = 2$, which means that the field decays in time as

$$\Phi = A/t^{2\ell+3} + B/t^{2\ell+5}. \tag{3.9}$$

It is clear that fitting the data to the simple term A/t^{μ} does not yield the theoretical value of $\mu = -(2\ell + 3)$. Correction terms of order $t^{-(\mu+1)}$ and $t^{-(\mu+3)}$ do not determine the value of μ as close to $-(2\ell + 3)$ as the correction $t^{-(\mu+2)}$ does.

This result supports the model proposed by Poisson [10] for the radiative falloff of a scalar field in a stationary, asymptotically flat and weakly curved spacetime. He shows that the first correction to the power-law tail is of order $t^{-(2\ell+5)}$. Our observation point is located at $r^* = 20M$. This result supports the general idea that gravitational and scalar field perturbations behave in similar ways. This similarity can also be verified in the case in which time-symmetric initial data is used in the simulation. In the scalar case it is enough to make the time derivative of the field equal to zero at $t = 0$. For the gravitational case, time symmetry implies that the extrinsic curvature is zero at $t = 0$. Such requirement is satisfied by choosing, for instance, the initial data as

$$\psi_4\big|_{t=0}^{\ell=2,m=0} = -\frac{(1 - 2M/r)}{2r^2}\left(\frac{M}{2R + M}\right)\left(\frac{z_0}{R}\right)^2 3\sin^2(\theta),$$

$$\text{with} \quad R = \frac{1}{4}(\sqrt{r} + \sqrt{r - 2M})^2, \quad \text{and} \tag{3.10}$$

$$\partial_t\psi_4\big|_{t=0}^{\ell=2,m=0} = -\left(\frac{2M}{r^2}\right)\psi_4\big|_{t=0}^{\ell=2,m=0} \tag{3.11}$$

corresponding to the close limit of two black holes (initially separated by $2z_0$ in conformal space) in a head-on collision [26].

TABLE IV. Power-law tails computed using a nonlinear fit of the form $\Phi = A/t^{\mu} + B/t^{\mu+n}$, for $n = 0, 1, 2, 3$. The last four columns show the value of μ for different values of the power correction n ($a = 0$ in these cases).

Domain:	$-50M \leq r^* \leq 950M$
Resolutions:	$\delta r^* = \{1, 2/3, 4/9, 8/27\}M$, $\delta\theta = \pi/8, \pi/12, \pi/18, \pi/27$,
Physical parameters:	$a = 0, \ell = 2, m = 0, s = -2$
Initial data:	outgoing Gaussian pulse

ℓ	m	predicted μ	$O(t^{\mu})$	$O(t^{\mu+1})$	$O(t^{\mu+2})$	$O(t^{\mu+3})$
2	0	7	7.642	7.130	7.062	7.303
	1		7.642	7.115	7.062	7.303
	2		7.642	7.125	7.062	7.303
3	0	9	10.15	9.675	9.024	9.393
	1		10.15	9.642	9.052	9.342
	2		10.15	9.643	9.058	9.385
	3		10.29	9.783	9.033	9.197
4	0	11	12.24	10.919	11.017	11.040
	1		13.18	11.695	10.977	10.907
	2		10.15	10.896	10.961	11.273
	3		10.91	11.011	11.037	11.052
	4		10.93	11.034	11.029	11.111

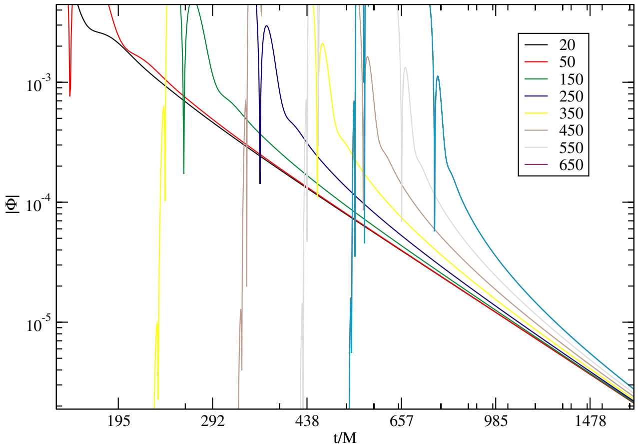

FIG. 10 (color online). Power-law tails, scalar case, $s = 0$, $\ell = 0$, $m = 0$. Observer's position is in M units.

The result of evolving time-symmetric initial data is a decrease of the power-law tail by one unit. For this we did the same runs and data fits as before, with the only difference that initial data is time-symmetric. The overall result is that for both, the scalar and gravitational cases, the power-law tail goes as $t^{-(2\ell+4)}$

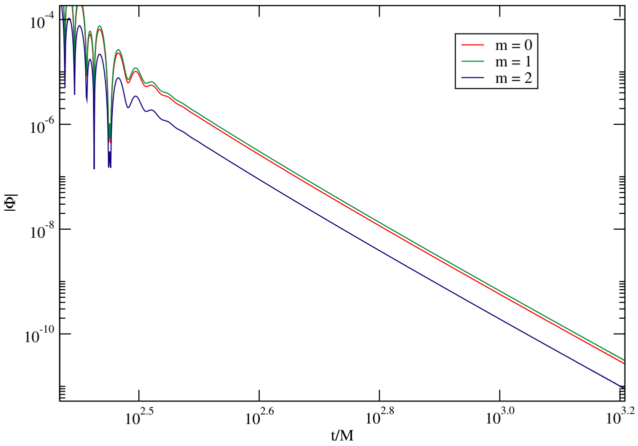

FIG. 11 (color online). Power-law tail $\ell = 2$, $m = 0, 1, 2$, $a = 0$.

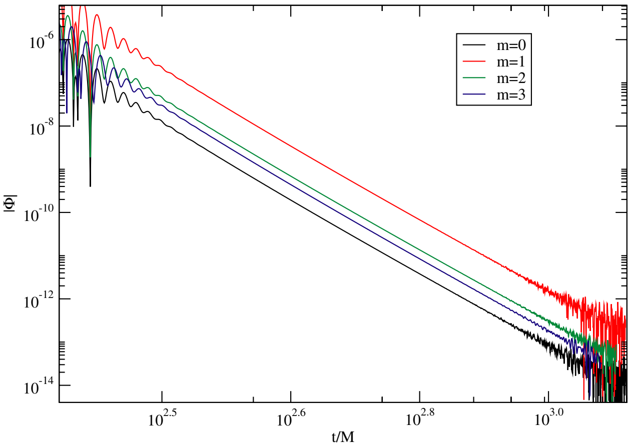

FIG. 12 (color online). Power-law tail $\ell = 3$, $m = 0, 1, 2, 3$, $a = 0$.

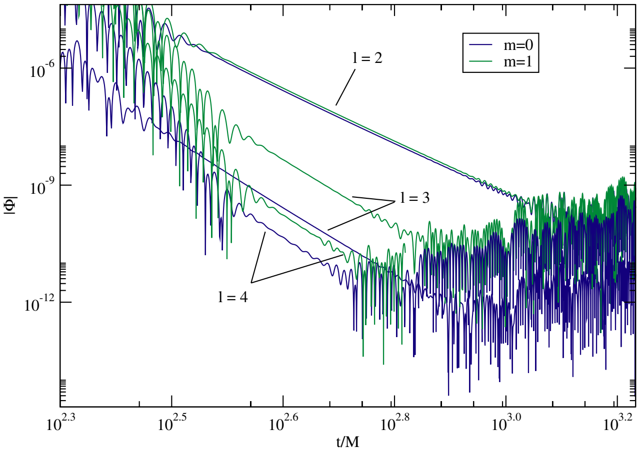

FIG. 14 (color online). Power-law tails for $a = 0.5$.

Figure 10 shows the exponential falloff for $s = 0$ at different distances from the black hole as a function of time. All of them approach asymptotically to the theoretically known value, 3. Figure 11 shows the evolution of gravitational perturbations for the $\ell = 2$ multipole for different values of m. In these cases we see no presence of round-off error because it has the slowest decay rate, $\Phi \propto t^{-7}$. In Fig. 12 we see the same situation as above but for $\ell = 3$. The power-law has a behavior $\Phi \propto t^{-9}$. Round-off error appears at $\Phi \sim 10^{-12}$. Finally in Fig. 13 round-off error appears approximately at the same value of Φ as in the previous case. We note that the quasinormal ringing is relatively short. In all the runs we use outgoinglike initial data as prescribed in (3.1).

So far we have been considering power-law tails for the case of a nonrotating black hole ($a = 0$). Figure 14 shows the power-law tails for the case in which $a = 0.5$ and for $\ell = 2, 3, 4$. We see that for some values of ℓ the duration of the tail is too short for an accurate determination of the power law. Doing a nonlinear fitting for the case $\ell = 2$, we found a tail power of -7.0011. For the other cases, this very short tail phase is not enough to tell with certainty the power-law exponent; besides, the tail has still some small oscillation in that time interval. To verify the effects of a Kerr background in the evolution of the gravitational perturbations, the frequencies of the quasinormal ringing provide an useful test; as shown in the next section.

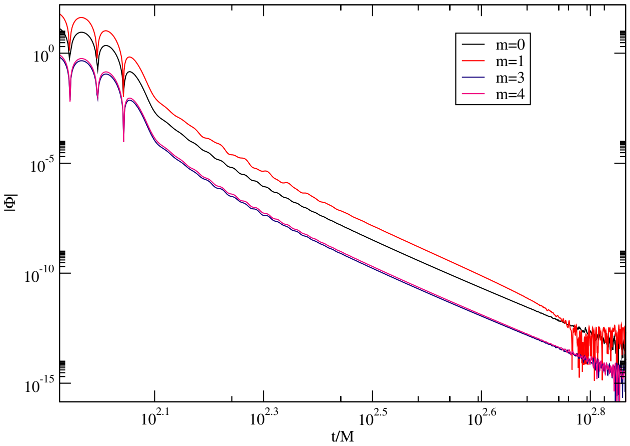

FIG. 13 (color online). Power-law tail $\ell = 4$, $m = 0, 1, 3, 4$, $a = 0$.

D. Quasinormal modes

We compute the quasinormal mode frequencies for the cases shown in Fig. 14, which correspond to the Kerr spacetime with $a = 0.5$ (Table V). The case $\ell = 2$ agrees with the known frequencies [27,28] within an error of less than 1%. For the cases $\ell = 3$ and $\ell = 4$ we get frequencies similar to the $\ell = 2$ multipole due to mode mixing. We also compute these frequencies for the case of a Schwarzschild spacetime (Table VI). In this case, the frequency values agree with the predicted ones [29–31] within a 0.1 to 1.4% error (In the cases for $\ell = 4$, the numerical evolution was not able to render a clear quasinormal ringing.)

Finally, Figs. 15 and 16 show the evolution for $m = 0$ of $\ell = 3$ and $\ell = 4$ respectively, for different values of a. We can see that the power-law tail is roughly the same for each

TABLE V. Quasinormal mode frequencies for $a = 0.5$ (NA = not available).

ℓ	m	computed σM	predicted σM
2	0	$0.384 + 0.0875i$	$0.3833 + 0.08\,707i$
2	1	$0.341 + 0.0805i$	$0.4206 + 0.08\,617i$
3	0	NA $+0.0800i$	$0.61212 + 0.09\,077i$
3	1	$0.339 + 0.0803i$	$0.65060 + 0.0900i$
4	0	$0.382 + 0.0860i$	NA
4	1	$0.341 + 0.0797i$	NA

TABLE VI. Quasinormal mode frequencies for $a = 0$.

ℓ	m	σM	predicted σM
2	0	$0.373 + 0.0875i$	$0.3\,736\,715 + 0.0\,889\,625i$
2	1	$0.375 + 0.0869i$	$0.3\,736\,715 + 0.0\,889\,625i$
2	2	$0.376 + 0.0877i$	$0.3\,736\,715 + 0.0\,889\,625i$
3	0	$0.601 + 0.0903i$	$0.5\,994\,435 + 0.092\,703i$
3	1	$0.600 + 0.0902i$	$0.5\,994\,435 + 0.092\,703i$
3	2	$0.605 + 0.0901i$	$0.5\,994\,435 + 0.092\,703i$
3	3	$0.598 + 0.0933i$	$0.5\,994\,435 + 0.092\,703i$

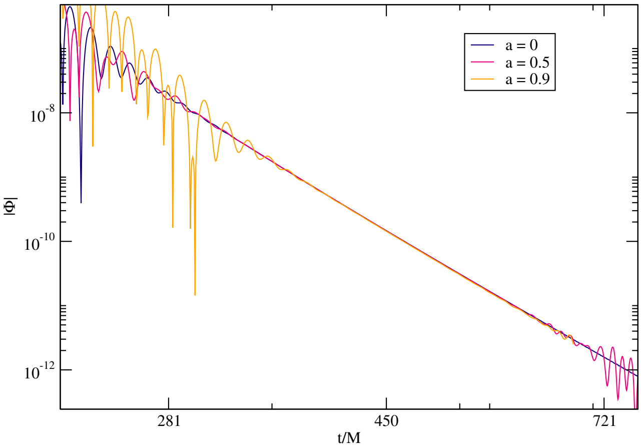

FIG. 15 (color online). Power-law tail $\ell = 3$, $m = 0$, $a = 0, 0.5, 0.9$.

case and that multipole conversion to the lowest multipole is present.

E. Fourth order versus second order

We can say that the advantage of using a fourth-order convergent code is that we can achieve the same results of the second-order one with less resolution. In other words, the same degree of accuracy can be obtained with both approaches in the same computational domain but the second-order one will need more points. Quantitatively, we can compare the error in the solution for both cases. This error is the difference between the true solution and the numerical solution for a given resolution. If we denote this quantity by e_h, where h is the grid spacing then we have

$$e_h = k_n h^n, \tag{3.12}$$

where $k = k(r, \theta)$ and n is the order of accuracy. If we equate the errors for $n = 2$ and $n = 4$, the relationship between resolutions is

$$h_2 = \sqrt{\frac{k_4}{k_2}} h_4^2. \tag{3.13}$$

If in the fourth-order method we increase the resolution by a factor ten, $h_4 = h/10$, then the equivalent resolution in the second-order one is approximately 10 times bigger, i.e. $h_2 = h/100$. This implies that in a one dimensional problem the number of points has also to be 10 times bigger. If a two dimensional problem is considered then the second-order grid should contain 100 times more points than that of the fourth-order method, to get the same error in the solution.

A feature of the finite differences methods is that according to (3.12), if we increase resolution by some factor c the error is reduced by a factor c^n. Thus each time we double resolution, the error decreases by a factor of 4 in the second-order method and by 16 in the fourth-order method.

The above considerations put the fourth-order method in a better position than the second-order one but, as we said in the introduction, the price we have to pay is running time. Given a resolution h, the fourth-order method will find a more accurate solution than the second-order one. The time that the fourth-order method will take will be longer because there are much more calculations to be done. In order to determine if the gain in a smaller grid is greater than the loss in running time, we did some numerical experiments. The running time $t_{\rm run}$ is given approximately by

$$t_{\rm run} \sim \frac{\delta\theta_0}{\delta\theta} \left(\frac{\delta r_0^*}{\delta r^*}\right)^2 t_0, \tag{3.14}$$

where t_0 is the running time at resolutions δr_0^* and $\delta\theta_0$. Fixing $\delta r_0^* = 1$ and $\delta\theta_0 = \pi/8$, $t_0 = 16.3$ min in the case of the fourth-order method; and $t_0 = 3.5$ min for the second-order one (we used a Pentium 4 CPU 2.4 GHz). These times correspond to the gravitational case $\ell = 2$, $m = 0$ in an interval $-50 < r^* < 950M$ being the simulation time $1600M$. In this simulation, the fourth-order method gave very good results whereas the second-order one becomes unstable around $t = 300M$. In order to obtain the same result (power-law tail) than the fourth-order one, it was necessary the increase the resolution 4 times in both

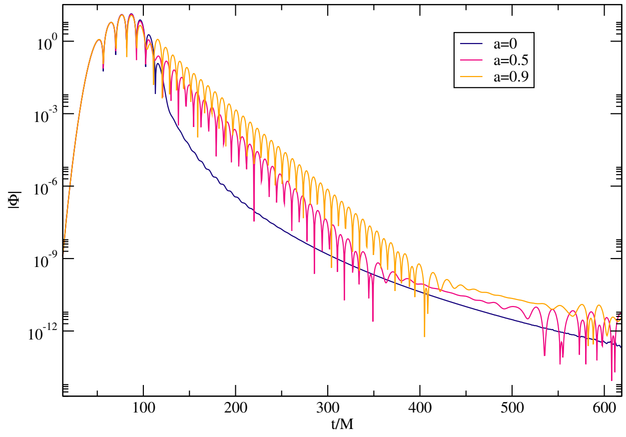

FIG. 16 (color online). Power-law tail $\ell = 4$, $m = 0$, $a = 0, 0.5, 0.9$.

TABLE VII. RAM memory used for various grid sizes for second and fourth-order methods.

RAM memory [Mb]			running time [hrs]	
$N_r \times N_\theta$	2nd order	4th order	2nd order[a]	4th order
1000×8	19	22	0.06	0.25
2000×16	64	71	0.48	2
4000×32	236	249	3.73	16

[a] These times are for equal grid sizes. For equivalent resolutions, the running time for the second-order method is approximately 14 times larger than that of the fourth-order method.

directions. This implies that now, the running time for the second-order method is $t_{\text{run}} \sim 230\,\text{min}$. This time is 14 times larger than that corresponding to the fourth-order method. So we definitely have a gain in speed, when the errors in the numerical solutions (for both methods) are kept equal.

As to the RAM memory, Table VII gives information about the amount of memory used in function of the grid size ($N_r \times N_\theta$). These values depend on the coding details of the algorithm. In this kind of problem, computer memory is not such a crucial factor as it is the speed.

IV. CONCLUSIONS

The main goal of this research has been to implement a stable fourth-order accurate method to numerically integrate the Teukolsky equation for gravitational perturbations in the time domain. In order to verify and evaluate the efficiency of our fourth-order method, we have reproduced the main known results, i.e. power-law tails and quasinormal ringing. Power-law tails is a subject in which there are still unsolved questions concerning the late time behavior of the perturbations and its dependence on the coordinates and the initial data [10]. We addressed some of these issues here (such as the confirmation of the dependence of the exponent on the initial data and the nonleading power), and others are left for future research. We studied the case of time-symmetric initial initial data. We have been able to confirm in this case that the late time behavior agrees well with the predicted $\sim 1/t^{2\ell+4}$ decay [11]. We have also confirmed numerically that for an observer located far away from the hole ($r_{\text{Obs}} > 20M$) we see the predicted $\sim A/t^{2\ell+3} + B/t^{2\ell+5}$ correction to the power law [10]. This was verified for both, the scalar and gravitational perturbations.

The fourth-order method implemented in this work has shown to be convergent and stable in all runs we did. The ansatz proposed by Krivan *et al.* [12] effectively removes the growing in time of the field, a feature that is expected from the asymptotic behavior of the solutions. When carrying out our calculation, we noticed that the coefficients of the Teukolsky equation reported in the appendix of [12] do not correspond to those we got when the same ansatz there proposed is used. Instead, they correspond to an ansatz without the r^3 factor (see Eq. (2.3)). We also verify that the formulation of the Teukolsky equation as a system of first-order differential equations is a powerful technique because it allows to express the first time derivative as a function of the spatial derivatives. The resulting system of equations has the form of the advection equation. That was the key idea that allowed us to implement a fourth-order method to solve the equation: expand the solution in a power series of time keeping terms up to fourth order and then use the differential equation to substitute the time derivatives by spatial derivatives. Using this procedure, a higher order method could be developed in a straightforward manner. A local stability analysis leads to a Courant factor of 1.5 below which we can perform stable evolutions for the nonrotating case [see Appendix A.]

The time evolutions carried out with the fourth-order method yielded accurate results even when relatively low resolutions were used. The lowest resolution was $\delta r^* = 1$, $\delta\theta = \pi/8$ for the $\ell = 2$, $m = 0$ case. The highest resolution used was $\delta r^* = 0.125$ and $\delta\theta = \pi/48$, for the $\ell = 4$ multipole. In finite difference methods the resolution is chosen in such a way that the details of the profiles of the functions involved in the calculations can be accurately approximated. For higher values of ℓ, the θ-dependence has more oscillations in its domain therefore more points are needed to find a reliable solution. The more oscillations or narrow peaks a function has the more resolution we need. This comes from the fact that those functions have derivatives whose values oscillate rapidly and higher derivatives vary even faster. If the resolution is not good enough the effect is a "numerical mode mixing", that has nothing to do with the physical model, but with the numerical aspects of the implementation. This mode mixing acts like if we were evolving the waves in a Kerr background, where physics tells us that angular mode mixing is expected. This unwanted effect cannot be easily detected when $a \neq 0$ in the simulations. Therefore it is absolutely necessary to verify that this effect is not present when we evolve in the Schwarzschild background, where the physical mode mixing does not occur. This may explain some discrepancy on the computed power-law exponent decay appeared in the literature.

For $a \neq 0$ Table V shows clearly that for $\ell = 3, 4, ..$ the mode mixing acts bringing down the quasinormal frequencies close to that of the $\ell = 2$. The same effect is observed in the tails' power, although it is more difficult to prove (See Fig. 14).

Boundary conditions were not a particular issue of concern in this research. The radial inner boundary was not a problem because the field decays exponentially near that region (for $s = -2$). The radial outer boundary always reflects part of the wave. The immediate solution is to push this boundary far away such that this reflection does not interfere in the region of interest. A refinement of the boundary conditions will be needed when a large computational domain can not be used in favor of higher resolutions [32].

In summary, we have a reliable computational tool to explore several interesting problems concerning first-order perturbations of black holes. We shed some light on the late time behavior of gravitational and scalar fields in a Schwarzschild and Kerr background. This is a problem that has been studied both analytically and numerically in recent years and future applications include the problem of the orbiting particle around a rotating black hole, and second-order perturbations in the close limit approximation to two colliding black holes [15].

ACKNOWLEDGMENTS

We are very grateful to E. Poisson for useful discussions on power-law tails, and to K. Kokkotas for making available unpublished values of the quasinormal frequencies for rotating black holes. We also gratefully acknowledge the support of the NASA Center for Gravitational Wave Astronomy at The University of Texas at Brownsville (NAG5-13396) and to NSF from Grant Nos. PHY-0140326 and PHY-0354867.

APPENDIX A: STABILITY ANALYSIS

We apply now a von Neumann stability analysis to our fourth-order scheme derived in Sec. II C. This analysis is local, which means that we assume that the coefficients of the finite difference equation vary slowly in space and time (In our case, these coefficients do not depend on time.) such that they can be considered to be constant. We say that the method is stable if the scheme is stable for every (constant) value of the coefficients in their range [33]. The idea is to expand the solution of the difference equation in its eigenmodes $e^{i.k.j.\delta x}$. The time dependence of these modes is a succession of powers of some complex number $\xi(k)$, called *amplification factor*. With this, we say that the difference equation is stable if $|\xi(k)| \leq 1$, for a given value of k. The eigenmodes of the difference Eq. (2.54) can be written as [21]

$$U_j^n = \xi^n e^{i.k.j.\delta x}, \tag{A1}$$

where $\xi = \xi(k)$ is a complex quantity, k is a real wave number, $j = 0, \ldots, N$, labels the grid points, and δx is the spatial resolution. Substituting (A1) into (2.54) we get a first grade polynomial in ξ. After some algebra we get

$$\begin{aligned}\xi(k) = {}& 1 + \frac{1}{3}\alpha^2(\cos k\delta x - 7)\sin^2\frac{k\delta x}{2} - \frac{2}{9}\alpha^4(\cos k\delta x - 4) \\ & \times \sin^4\frac{k\delta x}{2} + i\bigg[\frac{1}{6}\alpha(8\sin k\delta x - \sin 2k\delta x) \\ & + \frac{1}{24}\alpha^3(8\sin 2k\delta x - 13\sin k\delta x - \sin 3k\delta x)\bigg],\end{aligned} \tag{A2}$$

or

$$\begin{aligned}|\xi(k)|^2 = {}& 1 + \frac{8}{9}\alpha^2(\cos k\delta x - 5)\sin^6\frac{k\delta x}{2} - \frac{4}{9}\alpha^4(4\cos k\delta x \\ & - 17)\sin^8\frac{k\delta x}{2} + \frac{1}{54}\alpha^6(133\cos k\delta x \\ & - 34\cos 2k\delta x + 3\cos 3k\delta x - 150)\sin^6\frac{k\delta x}{2} \\ & + \frac{4}{81}\alpha^8(\cos k\delta x - 4)^2\sin^8\frac{k\delta x}{2},\end{aligned} \tag{A3}$$

where $\alpha = v\delta t/\delta x$ is the Courant factor.

This is a periodic function with a period of 2π. For the scheme to be stable it has to satisfy the stability condition

$$|\xi| \leq 1. \tag{A4}$$

Although we can find analytic solutions for this equation, just to present them here would occupy over a page. Rather than analytic solutions, we are interested in some interval of values for α, such that our fourth-order method is stable. The behavior of $|\xi|^2$ as a function of k is shown in Fig. 17 for some values of α. With certainty, we can conclude that ξ is less than 1 for $\alpha \leq 1.5$. This implies that the Courant condition for this case is

$$v\delta t \leq 1.5\delta x. \tag{A5}$$

This value is 50% greater than that required by the second-order Lax-Wendroff method and many others. This can be understood by expanding the amplification factor $\xi(k)$ in series of $k\delta x$. In practice δx must be small enough to correctly approximate the continuous differential equation. This means that for modes corresponding to small values of k we can expand (A3) in a power series of $k\delta x$. That is

$$|\xi|^2 = 1 - \left(\frac{\alpha^2}{18} + \frac{\alpha^6}{72}\right)(k\delta x)^6 + O((k\delta x)^8). \tag{A6}$$

It is interesting to compare this with the corresponding series expansion of $|\xi|^2$ for the Lax and Lax-Wendroff methods. For the Lax method we find [21]

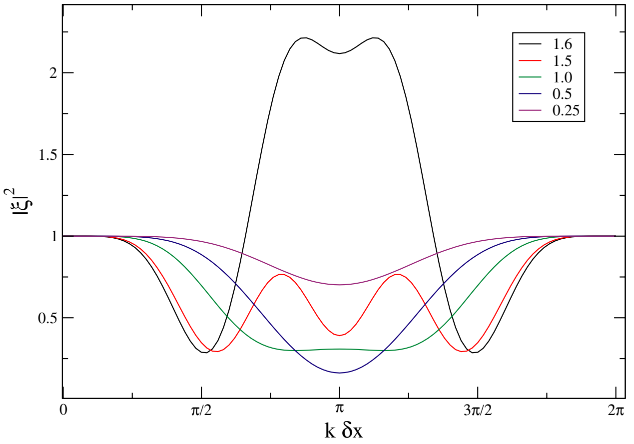

FIG. 17 (color online). $|\xi|^2$ vs $k\delta x$ for several values of α.

$$|\xi|^2 = 1 - (1 - \alpha^2)(k\delta x)^2 + \cdots \tag{A7}$$

and for the Lax-Wendroff method we have

$$|\xi|^2 = 1 - \alpha^2(1 - \alpha^2)\frac{(k\delta x)^4}{4} + \cdots. \tag{A8}$$

We can see that our fourth-order method has a sixth order dependence of $k\delta x$, which means that mode damping effects become relevant for much higher values of k, making this method more accurate. The generalization of the scheme to two dimensions is illustrated in the subsection 3. In this case the situation is more complicated because we are taking first and second derivatives in the θ direction. We were not able to find an analytic Courant factor that took into account the θ direction. From numerical experiments we verified that the ratio of time to spatial integration steps (based on the Courant condition) used in [12] for the second-order algorithm, produced stable runs in our case too. Thus, as a rule of thumbs, we always kept $\delta t = \min(\delta r^*, 5\delta\theta)$.

APPENDIX B: FOURTH-ORDER ACCURATE DERIVATIVES

This are the formulas to compute fourth-order accurate derivatives using finite differences. Those which are centered have always less truncation error than the corresponding off-centered ones. In all of them, h is the size of the step and $x \le \xi \le x + h$. We neglect term of powers higher than four.

(1) First derivative

- (a) centered

$$u'(x) = \frac{u_{j-2} - 8u_{j-1} + 8u_{j+1} - u_{j+2}}{12h} - \frac{1}{30}h^4u^{(5)}(\xi) \tag{B1}$$

- (b) off-centered (1 point)

$$u'(x) = \frac{-3u_{j-1} - 10u_j + 18u_{j+1} - 6u_{j+2} + u_{j+3}}{12h} + \frac{1}{20}h^4u^{(5)}(\xi) \tag{B2}$$

- (c) off-centered (2 points)

$$u'(x) = \frac{-25u_j + 48u_{j+1} - 36u_{j+2} + 16u_{j+3} - 3u_{j+4}}{12h} - \frac{1}{5}h^4u^{(5)}(\xi) \tag{B3}$$

(2) Second derivative

- (a) centered

$$u''(x) = \frac{-u_{j-2} + 16u_{j-1} - 30u_j + 16u_{j+1} - u_{j+2}}{12h^2} - \frac{1}{90}h^4u^{(6)}(\xi) \tag{B4}$$

- (b) off-centered (1 point)

$$u''(x) = \frac{10u_{j-1} - 15u_j - 4u_{j+1} + 14u_{j+2} - 6u_{j+3} + u_{j+4}}{12h^2} - \frac{13}{180}h^4u^{(6)}(\xi) \tag{B5}$$

- (c) off-centered (2 points)

$$u''(x) = \frac{45u_j - 154u_{j+1} + 214u_{j+2} - 156u_{j+3} + 61u_{j+4} - 10u_{j+5}}{12h^2} - \frac{137}{180}h^4u^{(6)}(\xi) \tag{B6}$$

(3) Third derivative

- (a) centered

$$u'''(x) = \frac{u_{j-3} - 8u_{j-2} + 13u_{j-1} - 13u_{j+1} + 8u_{j+2} - u_{j+3}}{8h^3} - \frac{7}{120}h^4u^{(7)}(\xi) \tag{B7}$$

- (b) off-centered (1 point)

$$u'''(x) = \frac{-u_{j-2} - 8u_{j-1} + 35u_j - 48u_{j+1} + 29u_{j+2} - 8u_{j+3} + u_{j+4}}{8h^3} + \frac{1}{15}h^4u^{(7)}(\xi) \tag{B8}$$

- (c) off-centered (2 points)

$$u'''(x) = \frac{-15u_{j-1} + 56u_j - 83u_{j+1} + 64u_{j+2} - 29u_{j+3} + 8u_{j+4} - u_{j+5}}{8h^3} - \frac{7}{120}h^4u^{(7)}(\xi) \tag{B9}$$

- (d) off-centered (3 points)

$$u'''(x) = \frac{-49u_j + 232u_{j+1} - 461u_{j+2} + 496u_{j+3} - 307u_{j+4} + 104u_{j+5}}{8h^3} - \frac{15u_{j+6}}{8h^3} + \frac{29}{15}h^4u^{(7)}(\xi) \quad \text{(B10)}$$

(4) Fourth derivative
   (a) centered

$$u^{(4)}(x) = \frac{-u_{j-3} + 12u_{j-2} - 39u_{j-1} + 56u_j - 39u_{j+1} + 12u_{j+2} - u_{j+3}}{6h^4} - \frac{7}{240}h^4u^{(8)}(\xi) \quad \text{(B11)}$$

   (b) off-centered (1 point)

$$u^{(4)}(x) = \frac{4u_{j-2} - 11u_{j-1} + 31u_{j+1} - 44u_{j+2} + 27u_{j+3} - 8u_{j+4} + u_{j+5}}{6h^4} + \frac{11}{80}h^4u^{(8)}(\xi) \quad \text{(B12)}$$

   (c) off-centered (2 point)

$$u^{(4)} = \frac{21u_{j-1} - 112u_j + 255u_{j+1} - 324u_{j+2} + 251u_{j+3} - 120u_{j+4}}{6h^4} + \frac{33u_{j+5} - 4u_{j+6}}{6h^4} - \frac{127}{240}h^4u^{(8)}(\xi) \quad \text{(B13)}$$

   (d) off-centered (3 points)

$$u^{(4)} = \frac{56u_j - 333u_{j+1} + 852u_{j+2} - 1219u_{j+3} + 1056u_{j+4} - 555u_{j+5}}{6h^4} + \frac{164u_{j+6} - 21u_{j+7}}{6h^4} - \frac{967}{240}h^4u^{(8)}(\xi) \quad \text{(B14)}$$

---

[1] J. G. Baker, M. Campanelli, and C. O. Lousto, Phys. Rev. D **65**, 044 001 (2002).

[2] J.G. Baker, M. Campanelli, C.O. Lousto, and R. Takahashi, Phys. Rev. D **65**, 124 012 (2002).

[3] J. Baker, M. Campanelli, C. O. Lousto, and R. Takahashi, Phys. Rev. D **69**, 027 505 (2004).

[4] J. Baker, B. Brügmann, M. Campanelli, and C. O. Lousto, Classical Quantum Gravity **17**, L149 (2000).

[5] J. Baker, B. Brügmann, M. Campanelli, C. O. Lousto, and R. Takahashi, Phys. Rev. Lett. **87**, 121 103 (2001).

[6] N. Andersson, Phys. Rev. D **55**, 468 (1997).

[7] R. Price, Phys. Rev. D **5**, 2419 (1972).

[8] E. Leaver, Phys. Rev. D **34**, 384(1986).

[9] E. Ching, P. Leung, W. Suen, and K. Young, Phys. Rev. D **52**, 2118 (1995).

[10] E. Poisson, Phys. Rev. D **66**, 044008 (2002).

[11] J. Karkowski, Z. Swierczynski, and E. Malec, Classical Quantum Gravity **21**, 1303 (2004).

[12] W. Krivan, P. Laguna, P. Papadopoulos, and N. Anderson, Phys. Rev. D **56**, 3395 (1997).

[13] E. Poisson, Phys. Rev. D **55**, 639 (1997).

[14] M. Campanelli and C. O. Lousto, Phys. Rev. D **56**, 6363 (1997).

[15] M. Campanelli and C. O. Lousto, Phys. Rev. D **59**, 124 022 (1999).

[16] C. O. Lousto, Phys. Rev. Lett. **84**, 5251 (2000).

[17] C. O. Lousto, Classical Quantum Gravity **22**, S369 (2005).

[18] Y. Zlochower, J. G. Baker, M. Campanelli, and C. O. Lousto, Phys. Rev. D **72**, 024 021 (2005).

[19] C. O. Lousto, Classical Quantum Gravity **22**, S543 (2005).

[20] S. Teukolsky, Astrophys. J. **185**, 635 (1973).

[21] W. H. Press, S. A. Teukolsky, W. T. Vetterling, and B. P. Fannery, *Numerical Recipes in C* (Cambridge University Press, Cambridge, England, 1999).

[22] W. Krivan, P. Laguna, and P. Papadopoulos, Phys. Rev. D **54**, 4728 (1996).

[23] D. Kincaid and W. Chaney, *Numerical Analysis: Mathematics of Scientific Computing* (Brooks-Cole, Belmont, 2002).

[24] M. A. Scheel *et al.*, Phys. Rev. D **69**, 104 006 (2004).

[25] L. Burko and A. Ori, Phys. Rev. D **56**, 7820 (1997).

[26] C. O. Lousto, Phys. Rev. D **63**, 047 504 (2001).

[27] E. Seidel and S. Iyer, Phys. Rev. D **41**, 374 (1990).

[28] K. D. Kokkotas, Classical Quantum Gravity **8**, 2217 (1991).

[29] E. Leaver, Proc. R. Soc. A **402**, 285 (1985).

[30] M. Giammatteo, gr-qc/0303011.

[31] N. Fröman, P. O. Fröman, N. Andersson, and A. Hökback, Phys. Rev. D **45**, 2609 (1992).

[32] S. R. Lau, gr-qc/0507140.

[33] G. Sewell, *Finite Differences, Finite Elements and PDE2D. (The Numerical Solution of Ordinary and Partial Differential Equations)* (Academic Press, New York, 1988), out of print.